Cell Reports Medicine, Volume *5*

Supplemental information

An immune cell map of human lung adenocarcinoma development reveals an anti-tumoral role of the Tfh-dependent tertiary lymphoid structure

Wei Liu, Wenhua You, Zhenwei Lan, Yijiu Ren, Shuangshu Gao, Shuchao Li, Wei-Wei Chen, Chunyu Huang, Yong Zeng, Nengming Xiao, Zeshuai Wang, Huikang Xie, Huan Ma, Yun Chen, Guangsuo Wang, Chang Chen, and Hanjie Li

Supplementary Materials for

A time-resolved immune cell map of human lung adenocarcinoma development reveals an anti-tumoral role of the Tfh-dependent tertiary lymphoid structure

Wei Liu *et al*.

Corresponding authors: Hanjie Li, hj.li@siat.ac.cn

The file includes:

Extended Materials and Methods

Supplementary Figure 1 to 7

SUPPLEMENTAL FIGURES

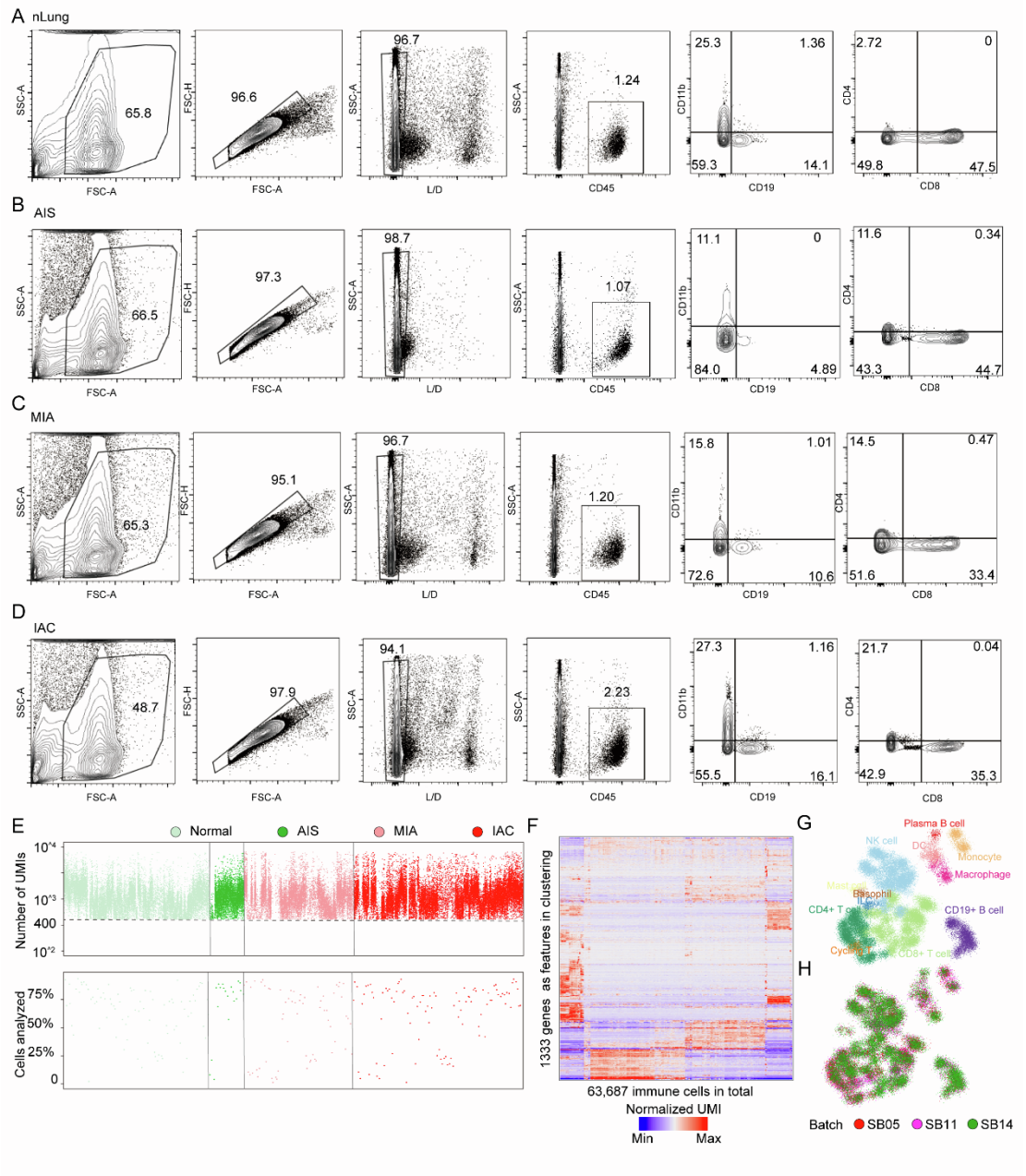

Supplementary Figure 1. The immune cell atlas in early-stage LUAD patients, related to Figure 1.

(A–D) Flow cytometry plots showing sorting strategy for the immune ($CD45^+$) after doublet exclusion from representative subjects (nLung, A; AIS, B; MIA, C; IAC, D). Plots were generated using FlowJo software (**STAR Methods**).

(E) Dot plots showing the number of UMIs and percentage of cells analyzed per batch of 384 wells (that were pooled for library construction, 380 cells and 4 empty controls) for all $CD45^+$ single immune cells from 93 samples (**STAR Methods**).

(F) Heatmap showing the clustering analysis of all 63,687 immune cells sorted from all the participants featuring normalized single-cell expression levels of a selected set of the most variable genes. Clustering is performed using 1,333 genes as features.

(G) 2D projection of detail-annotated immune cells. Annotated in twelve groups and marked by color code.

(H) 2D projection of subclustered immune cells from three sequence batches SB05, SB11 and SB14.

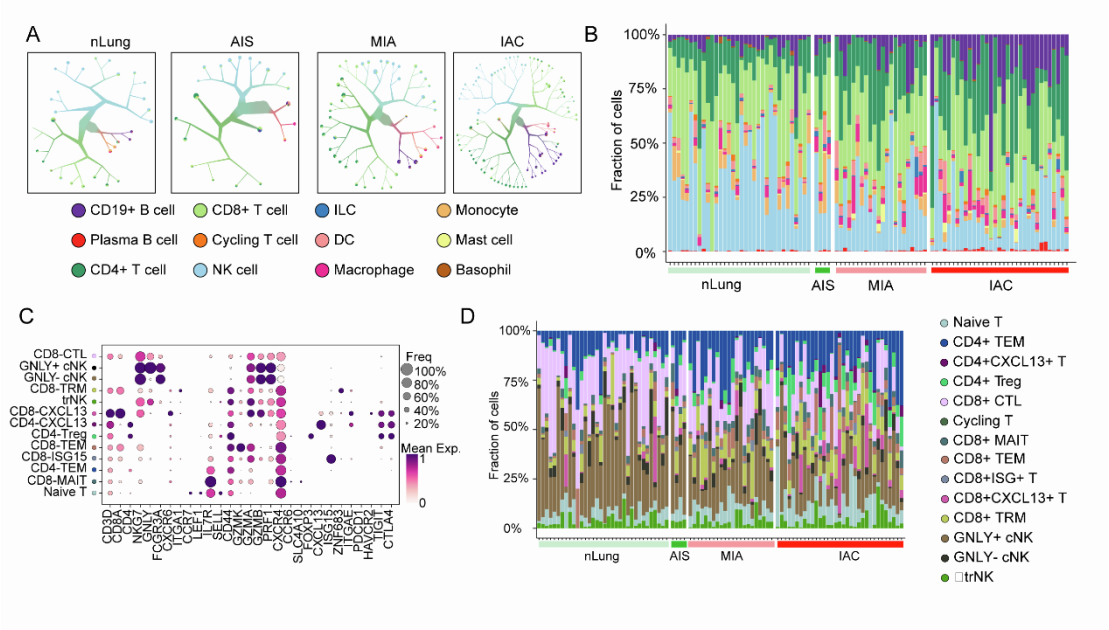

Supplementary Figure 2. Composition of immune cells at different stages of early-stage LUAD, related to Figure 2.

(A) The cell clustering by TooManyCells in nLung, AIS, MIA, and IAC are largely different (**STAR Methods**).

(B) Bar plots showing the immune cell-type composition within the nLung, AIS, MIA and IAC patients in the individual patients. Cell types are colored the same as in Figure 2A.

(C) Dot plot displaying key marker genes for T and NK cell clusters.

(D) Bar plots showing the T and NK cell-type composition within the nLung, AIS, MIA and IAC patients in the individual patients. Cell types are colored the same as in (Figure 2F).

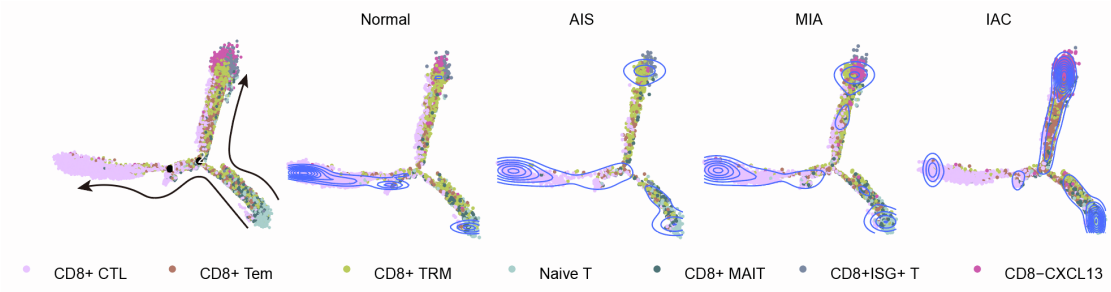

Supplementary Figure 3. Monocle trajectory inference of CD8$^+$ T cells, colored by their corresponding cell type, and displayed by tissue origins, related to Figure 2.

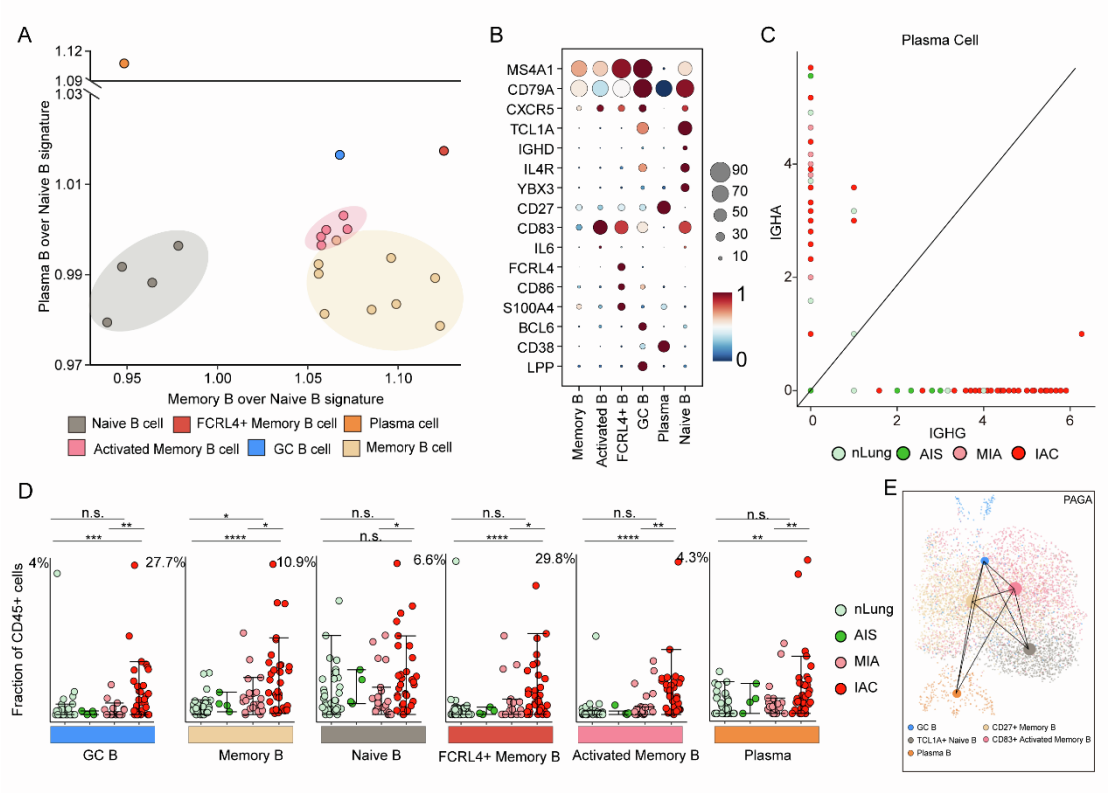

Supplementary Figure 4. Features of tumor-infiltrating B cell clusters, related to Figure 3.

(A) Bar graph showing memory B over naïve B signature versus plasma B over naïve B signature on CD19$^+$ B metacells.

(B) Expression of selected feature genes in B cell clusters.

(C) Scatter plot showing the expression of IgA and IgG in plasma cells.

(D) Dot plots showing percentages of B cell subpopulation in all CD45$^+$ cells within nLung, AIS, MIA and IAC patients. *p < 0.05, **p < 0.01, ***p < 0.001, Mann-Whitney U test, two-

sided. Error bars indicate mean ± SEM.

(E) PAGA analysis showing the potential developmental connectivity between different B cell subsets (**STAR Methods**).

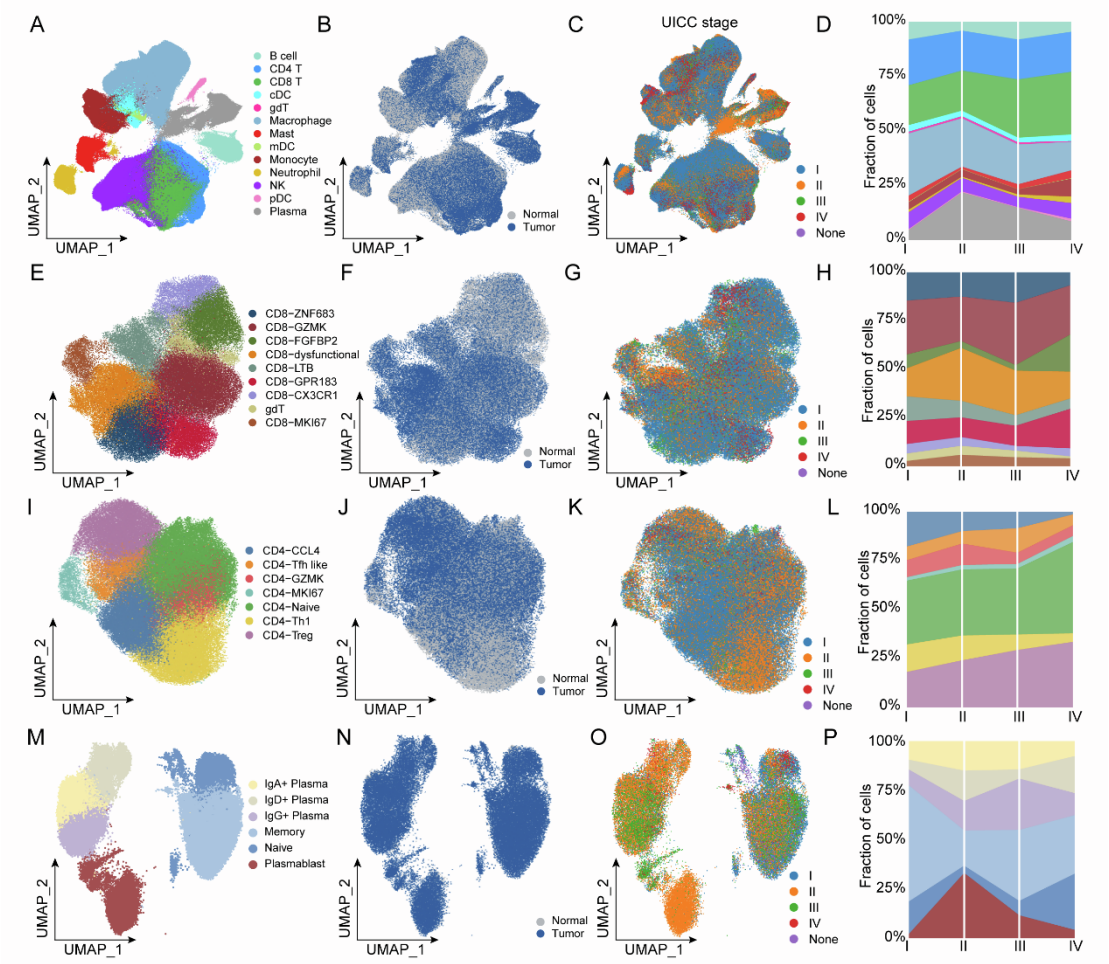

Supplementary Figure 5. Validation our scRNA-seq data by integrating published scRNA-seq data, related to Figure 1-3

(A-D) Overview of the immune cells as uniform manifold approximation and projection (UMAP) plots (A-C) and the fractions of tumor-infiltrating cell types in each stage (D) (see **Methods**).

(E-H) Overview of the CD8+ T cell populations as UMAP plots (E-G) and the fractions of tumor-infiltrating $CD8^+$ subclusters per stage (H).

(I-L) Overview of the $CD4^+$ T cell populations as UMAP plots (I-K) and the fractions of tumor-infiltrating $CD4^+$ T subclusters per stage (L).

(M-P) Overview of the B and plasma cell populations as UMAP plots (M-O) and the fractions

of tumor-infiltrating subclusters per stage (P).

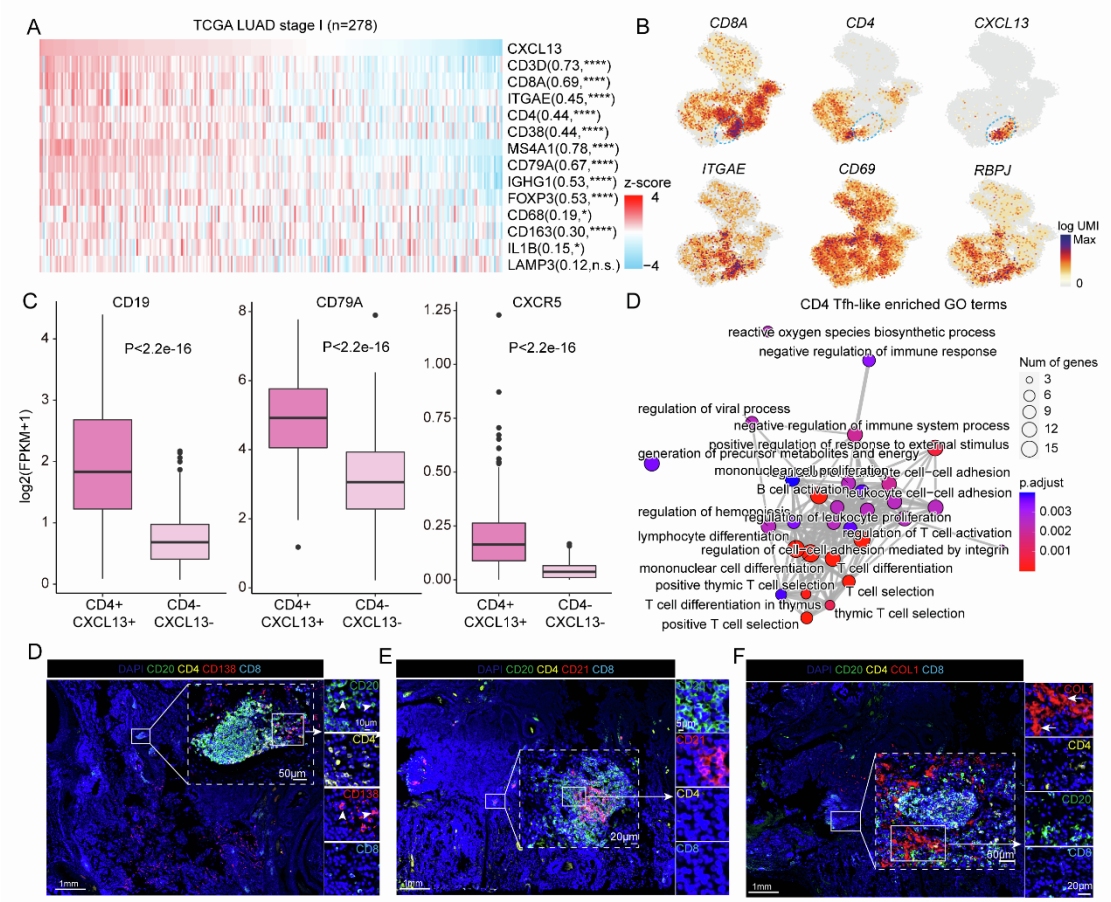

Supplementary Figure 6. Features and Dynamics of Tfh-like cells in early-stage LUAD, related Figure 4.

(A) The distribution of immune-associated genes into the IAC tumor site and *CXCL13* gene expression (n=278). Correlation was determined by Spearman's correlation test.

(B) 2D projection of subclustered nLung and tumor immune cells. Expression enrichment genes including *CD8A*, *CD4*, *CXCL13*, *ITGAE*, *CD69* and *RBPJ*.

(C) Box plots showing the expression of *CD19*, *CD79A* and *CXCR5* genes of TCGA patients with LUAD grouped by the expression levels of *CD4* and *CXCL13*. Expression level was measured by Log2 (FPKM+1).

(D) The enriched pathways for genes highly expressed in Tfh-like cells.

(E) Immunofluorescence images of LUAD patients stained for CD20, CD4, CD138, CD8 and the nuclei (DAPI, blue). The white arrows show plasma ($CD138^{+}$) cells. Scale bars, 1mm, 50 μm and 10μm.

(F) Immunofluorescence images of LUAD patients stained for CD20, CD4, CD21, CD8 and

the nuclei (DAPI, blue). The white arrows show fibroblasts ($CD21^+$) cells. Scale bars, 1mm, 20 μm and 5μm.

(G) Immunofluorescence images of LUAD patients stained for CD20, CD4, COL1, CD8 and the nuclei (DAPI, blue). The white arrows show FDC($COL1^+$) cells. Scale bars, 1mm, 50μm and 20 μm.

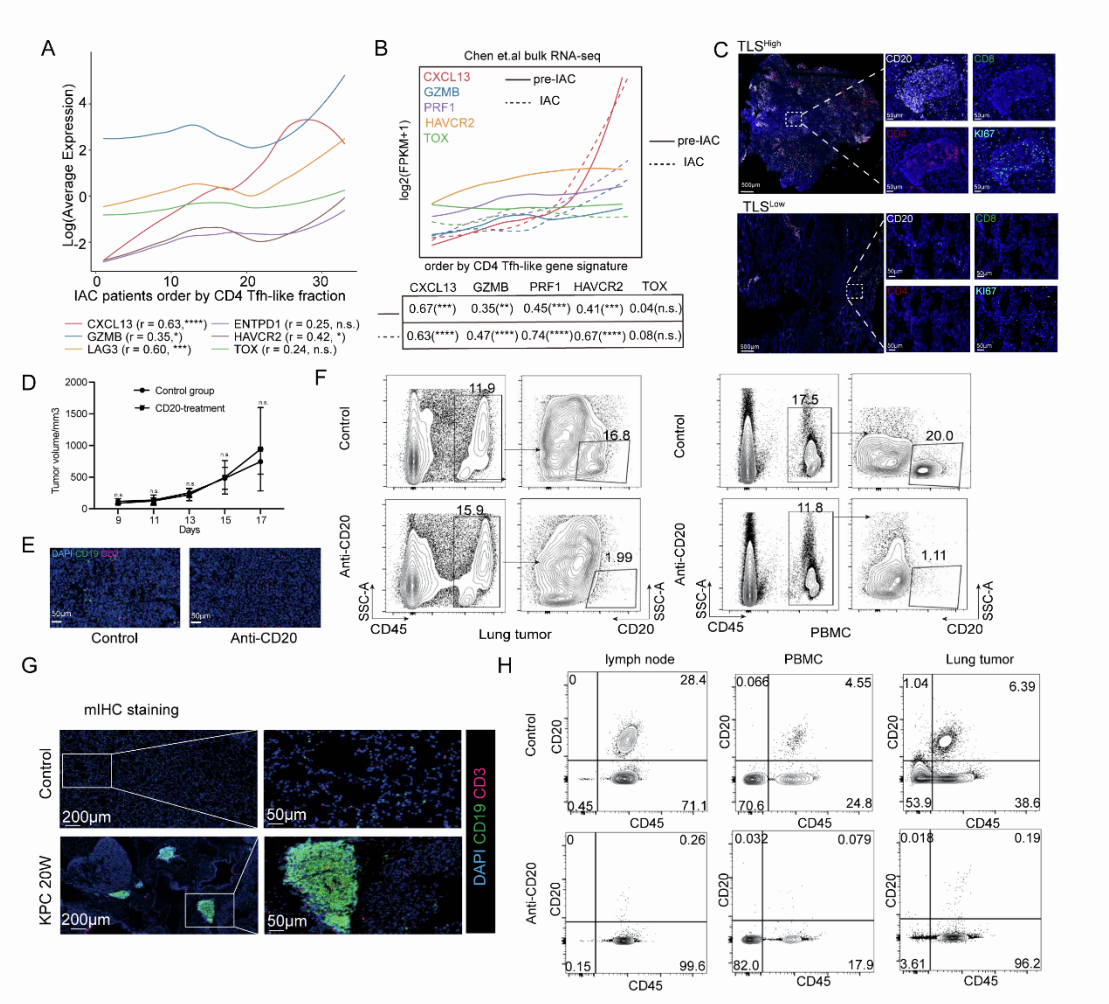

Supplementary Figure 7. The TLS plays an antitumor role, related Figure 6

(A) Expression of *CXCL13, GZMB, TOX, HAVCR2, LAG3*, and *ENTPD1* in $CD8^+$ T cells plotted along the fraction of Tfh-like cells. Data from n = 33 IAC tumors were summarized. P values were determined from Pearson correlation coefficient r, two-tailed linear regression t-test. ***$p < 0.001$.

(B) Expression of *CXCL13, GZMB, TOX, HAVCR2, PRF1* in IAC and pre-IAC RNA-seq data plotted along the Tfh-like cell signature score. P values were determined from Pearson

correlation coefficient r, two-tailed linear regression t-test. ***$p < 0.001$.

(C) Multiplex immunostaining assay of TLSs for the following markers: CD20, CD4, CD8, KI67 and DAPI in TLS^{high} and TLS^{low} patient. TLS^{high}, n=27, TLS^{low}, n=15. Scale bars, 500 μm and 50 μm.

(D) LLC were subcutaneously injected 8-week-old C57BL/6 mice followed by treatment with anti-CD20 antibody or PBS. The tumor size and image of tumor were obtained at 18 days. Control (n=8), anti-CD20 (n=8).

(E) Multiplex immunostaining assay of TLSs for the following markers: CD3, CD19 and DAPI in anti-CD20 treated LLC tumor-bearing mice. Scale bars, 50 μm.

(F) Flow cytometric analysis of $CD20^+$ B cells from lung tumor and PBMC of anti-CD20 treated LLC tumor-bearing mice compared with controls.

(G) Multiplex Immunostaining assay of TLSs for the following markers: CD3, CD19 and DAPI in KPCmice. Scale bars, 200 μm and 50 μm.

(H) Flow cytometric analysis of $CD20^+$ B cells from lymph node, PBMC and tumor samples of anti-CD20 treated KPC mice compared with controls.